

To appear in Proc. of the *8th International Astrophysics Conference*
“Shock Waves in Space and Astrophysical Environments,” (2010),
eds. X. Ao, R. Burrows & G. P. Zank (AIP Conf. Proc. 1183, New York).

Particle Acceleration at Relativistic Shocks in Extragalactic Systems

Matthew G. Baring¹ & Errol J. Summerlin^{1,2}

¹ *Department of Physics and Astronomy, MS-108, Rice University, P. O. Box 1892,
Houston, TX 77251-1892, USA* Email: baring@rice.edu

² *Heliospheric Physics Laboratory, Code 672, NASA's Goddard Space Flight Center,
Greenbelt, MD 20770, USA* Email: errol.summerlin@nasa.gov

Abstract. Diffusive shock acceleration (DSA) at relativistic shocks is expected to be an important acceleration mechanism in a variety of astrophysical objects including extragalactic jets in active galactic nuclei and gamma ray bursts. These sources remain strong and interesting candidate sites for the generation of ultra-high energy cosmic rays. In this paper, key predictions of DSA at relativistic shocks that are salient to the issue of cosmic ray ion and electron production are outlined. Results from a Monte Carlo simulation of such diffusive acceleration in test-particle, relativistic, oblique, MHD shocks are presented. Simulation output is described for both large angle and small angle scattering scenarios, and a variety of shock obliquities including superluminal regimes when the de Hoffman-Teller frame does not exist. The distribution function power-law indices compare favorably with results from other techniques. They are found to depend sensitively on the mean magnetic field orientation in the shock, and the nature of MHD turbulence that propagates along fields in shock environs. An interesting regime of flat spectrum generation is addressed, providing evidence for its origin being due to shock drift acceleration. The impact of these theoretical results on gamma-ray burst and blazar science is outlined. Specifically, *Fermi* gamma-ray observations of these cosmic sources are already providing significant constraints on important environmental quantities for relativistic shocks, namely the frequency of scattering and the level of field turbulence.

Keywords: Diffusive shock acceleration; hydromagnetic turbulence; gamma-ray bursts, active galactic nuclei, non-thermal emission

PACS: 98.70.Rz; 95.85.Pw; 98.70.Sa; 52.35.Ra; 52.25.Xz; 52.27.Ny; 52.35.Tc; 52.65.Pp

INTRODUCTION

There is bountiful evidence for efficient particle acceleration at collisionless shocks in the universe. The heliosphere, with its planetary bow shocks and traveling interplanetary shocks, has provided interesting and useful test cases for shock acceleration theories. In the remote regions of the universe, supersonic jets from active galactic nuclei (AGNs) and gamma-ray bursts (GRBs) have offered fascinating windows into an energetic part of the cosmos, where non-thermal radio waves, X-rays and gamma-rays abound. Fully understanding these sources mandates knowledge of how the particles that generate their light emission are energized. The foremost paradigms invoke acceleration at relativistic shocks. Radio imaging reveals very structured and time-variable jets in AGNs, rapid X-ray and gamma-ray variability in both blazar AGNs and GRBs suggest compact emission regions with relativistic bulk motions. Accordingly, comprehending the relationship between shock acceleration predictions and observations of these sources offers the key to elucidating the understanding of their environs; this constitutes the focus of this paper.

To effect this, an investigation of the features of diffusive shock acceleration is presented, using results from a test particle Monte Carlo simulation. Then the paper addresses probes of the acceleration theory parameter space imposed by extant GRB and blazar observations in high energy gamma-rays. The Monte Carlo approach [1, 2, 3, 4] is one of several major techniques devised to model particle acceleration at relativistic shocks; others include semi-analytic solutions of the diffusion-convection equation [6, 7, 8], and particle-in-cell (PIC) full plasma simulations [9, 10, 11, 12]. Each has its merits and limitations. Tractability of the analytic approaches generally restricts their solutions to power-law regimes for the phase space distributions $f(\mathbf{p})$. PIC codes are rich in their information on shock-layer electrodynamics and turbulence. However, to interface with astrophysical spectral data, a broad dynamic range in momenta is desirable, and this is the natural niche of Monte Carlo simulation techniques. A core property of acceleration at the relativistic shocks is that the distribution functions $f(\mathbf{p})$ are inherently anisotropic. This renders the power-law indices and other distribution characteristics sensitive to directional influences, such as the magnetic field orientation with respect to the shock normal, and the nature of MHD turbulence that often propagates along the field lines. These connections between observables and physical parameters of the shock environs are studied in some depth in this exposition.

DIFFUSIVE ACCELERATION AT RELATIVISTIC SHOCKS

The exploration of the properties of diffusive shock acceleration that is presented here employs the well-known kinematic Monte Carlo technique of Ellison and Jones that has been employed extensively in supernova remnant and heliospheric contexts, and is described in detail in numerous papers [1, 2, 13, 14, 15, 16]. Particles are injected upstream and allowed to convect into the shock, meanwhile diffusing in space so as to effect multiple shock crossings, and thereby gain energy through the shock drift and Fermi processes. In general, the upstream fluid frame magnetic field is inclined at an angle Θ_{Bfl} to the shock normal. The particles gyrate in laminar electromagnetic fields, with their trajectories being obtained by solving the Lorentz force equation in the normal incidence shock rest frame (NIF), where the upstream flow is incident along the shock normal (x -direction: see the left hand panel of Fig. 1 for the NIF shock geometry). In this frame, when $\Theta_{\text{Bfl}} > 0$, there is a $\mathbf{u} \times \mathbf{B}$ drift electric field in addition to the magnetic field. The effects of Alfvén wave and other hydromagnetic magnetic turbulence on particle propagation are modeled by phenomenologically scattering these ions elastically in the rest frame of the local fluid flow. This is generally applicable for high Alfvénic Mach number shocks. The simulation outputs particle fluxes and momentum and angular distributions, usually in the NIF, at any location upstream or downstream of the shock.

The simulation can routinely model diffusion incurred in particle interactions with MHD turbulence using either large-angle or small-angle scattering. At every scattering, the direction of the particle's momentum vector \mathbf{p} is deflected in the local fluid frame to a new value \mathbf{p}' . The scattering angle $\delta\theta = \cos^{-1}(\mathbf{p} \cdot \mathbf{p}' / |\mathbf{p}| |\mathbf{p}'|)$ is uniformly sampled within a solid angle $\delta\Omega$ up to a maximum deflection angle θ_{scatt} (see Figs. 2 and 3 of [2] for the scattering geometry). The time, δt_f , between scatterings in this frame is coupled [1] to the mean free path, λ , and θ_{scatt} , via $\delta t_f \approx \lambda \theta_{\text{scatt}}^2 / (6v)$ for particles

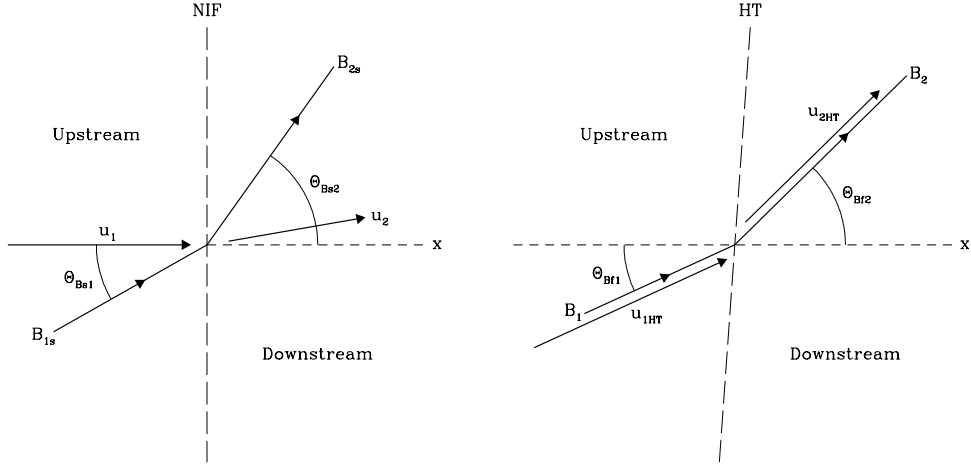


FIGURE 1. The geometry in the normal incidence (NIF; left panel) and de-Hoffmann Teller (HT; right panel) shock rest frames. Upstream flow speeds in the two reference frames are related by $u_{1\text{HT}} \equiv \beta_{1\text{HT}} c = u_1 / \cos \Theta_{\text{Bf1}}$. Upstream and downstream quantities are denoted by subscripts 1 and 2, respectively. In general, the NIF field angle Θ_{Bs1} differs from the fluid frame/HT frame value Θ_{Bf1} . Also, the shock plane in the HT frame is rotated from that in the NIF due to relativistic aberration effects.

of speed v . The resulting effect is that the gyrocenter of a particle with gyroradius r_g is shifted randomly by a distance of the order of $\theta_{\text{scatt}} r_g$ in the plane orthogonal to the local field. Accordingly, cross-field diffusion emerges naturally from the simulation. For large angle scattering (LAS, defined more precisely below), the scattering solid angle is $\theta_{\text{scatt}} \lesssim \pi$ steradians, and the transport is governed by kinetic theory [15, 17], where the ratio of the spatial diffusion coefficients parallel ($\kappa_{\parallel} = \lambda v/3$) and perpendicular (κ_{\perp}) to the mean magnetic field is given by $\kappa_{\perp}/\kappa_{\parallel} = 1/(1 + \eta^2)$. Here, the parameter $\eta = \lambda/r_g$ is the ratio of a particle's mean free path λ to its gyroradius r_g . As is often implemented for simplicity, in this work λ is assumed to be proportional to the particle momentum p , so that η is independent of p . This can be adjusted to accommodate other scattering laws as desired. Clearly, η controls the amount of cross-field diffusion, and is a measure of the level of turbulence present in the system, i.e. is an indicator of $\langle \delta B/B \rangle$. The Bohm limit of quasi-isotropic diffusion is realized when $\eta \sim 1$ and $\langle \delta B/B \rangle \sim 1$. This phenomenological description of diffusion in Monte Carlo techniques is most appropriate at high energies, and omits the details of microphysics present in plasma simulations such as PIC codes. In the injection domain at slightly suprathermal energies, the influences of complex turbulent and coherent electrodynamic effects become important, and will substantially modify the picture from pure diffusion.

It will become clear below that in oblique relativistic shocks, the diffusive transport of particles across the field, and hence across the shock, becomes critical to their retention in the acceleration process. Accordingly, for such systems, the interplay between the field angle Θ_{Bf1} and the value of λ/r_g controls the spectral index of the particle distribution [2, 5], a feature that is central to the interpretation of astrophysical source spectra. The phase space for acceleration theory results is now explored, before addressing their relevance to two classes of cosmic sources: gamma-ray bursts and blazars.

ACCELERATION SIGNATURES AT RELATIVISTIC SHOCKS

Diffusive particle acceleration at relativistic shocks naturally divides into two regimes: mildly-relativistic ($u_{1x} \lesssim c$) and ultra-relativistic ($u_{1x} \approx c$) systems. Hereafter, subscripts 1 denote upstream quantities. Neither regime is accessible to diagnostics via *in situ* particle measurements since the principal astrophysical sources possessing relativistic shocks exhibiting signatures of acceleration, namely pulsar wind termination shocks, jets in active galactic nuclei (blazars) and gamma-ray bursts, are so distant. An important property of diffusive acceleration at relativistic shocks that distinguishes them from their non-relativistic counterparts is their intrinsic anisotropy. This is driven by the powerful convective influence that enables efficient loss of particles away and downstream from the shock. The immediate consequence of this loss is a general difficulty in generating flat distributions of shock-accelerated particles, particularly for so-called superluminal ($\beta_{1x}/\cos\Theta_{\text{Bf1}} > 1$) relativistic discontinuities. These losses are muted somewhat in mildly-relativistic shocks, which are naturally expected in GRBs and perhaps also in blazars. Moreover, the resulting distributions $dN/dp \propto p^2 f(\mathbf{p})$ are more or less commensurate with those required to explain the radiation observations from these sources. Accordingly, this paper will study $\Gamma_1 = (1 - u_{1x}^2/c^2)^{-1/2} \sim 1 - 5$ shocks, focusing on the power-law tails $dN/dp \propto p^{-\sigma}$ realized at high momenta, where all memory of the injection momentum has been destroyed by diffusion. The array of possible distribution indices σ is highlighted, spawned by the sensitivity of both the energization in, and escape from, the shock layer, to (i) the size of the momentum deflection angle θ_{scatt} , (ii) the frequency or relative mean free path λ/r_g of scatterings, and (iii) the upstream field obliquity Θ_{Bf1} , a quantity connected to the global MHD structure of the shock.

The first effect, the dependence of σ on θ_{scatt} , has been documented in several recent papers [2, 4, 5], and will just be summarized here. When the diffusion in the shock layer samples large field fluctuations $\delta B/B \sim 1$ (seen, for example, in PIC simulations of relativistic shocks driven by the Weibel instability [9, 10, 11, 12]), it corresponds to large momentum deflections, delineating the regime of large angle scattering (LAS) with $4/\Gamma_1 \lesssim \theta_{\text{scatt}} \lesssim \pi$, where Γ_1 is the upstream flow's incoming Lorentz factor. This regime was first explored for $\Gamma_1 \lesssim 5$ by Ellison et al. [1]. Such large deflections produce huge gains in particle energy, of the order of Γ_1^2 , in successive shock crossings. These gains are kinematic in origin, and are akin to those in inverse Compton scattering. The result is an acceleration distribution dN/dp that is highly structured and much flatter on average [1] than p^{-2} for strong, parallel ($\Theta_{\text{Bf1}} = 0^\circ$), shocks, i.e. those with high sonic and Alfvénic Mach numbers. The bumpy structure is kinematic in origin, corresponding to sequential shock transits [18], and becomes more pronounced [2, 4, 5, 19] for large Γ_1 . For ultra-relativistic shocks, information of the injection momentum scale becomes insignificant when $p \gg mc$, and the bumps asymptotically relax to form a power-law distribution $dN/dp \propto p^{-\sigma}$, with an index in the range of $\sigma \sim 1.6$ [4]. From the plasma physics perspective, magnetic turbulence in relativistic shocks could easily be sufficient to effect scatterings on intermediate to large angular scales $\theta_{\text{scatt}} \gtrsim 1/\Gamma_1$, a proposition that becomes more enticing for ultra-relativistic shocks.

The principal focus in this paper is on particle distributions for $\theta_{\text{scatt}} \lesssim 1/\Gamma_1$ regimes, which are much smoother in appearance, and often necessarily steeper, at least for su-

perluminal regimes. The property of distribution smoothness meshes more easily with radiation spectral observations of extragalactic astrophysical sources, thereby motivating exploration of this portion of phase space. The kinematic energy gains in shock crossings are lowered considerably [18] when θ_{scatt} drops below this “Lorentz cone” angle $1/\Gamma_1$. Accordingly, the character of dN/dp and the particle anisotropy at the shock dichotomize, partitioned by the $\theta_{\text{scatt}} \sim 1/\Gamma_1$ boundary. Intermediate scattering angles $\theta_{\text{scatt}} \sim 1/\Gamma_1$ generate smooth distributions [4, 19], much like those for small angle scattering (SAS, often called pitch angle diffusion, PAD). The SAS regime has spawned the often cited asymptotic, ultrarelativistic index of $\sigma = 2.23$ for $dN/dp \propto p^{-\sigma}$ [8], first noticed in Monte Carlo simulations [20]. This special result, applicable in both shock rest and fluid frames for momenta $p \gg \Gamma_1 mc$, is realized only for parallel shocks with $\Theta_{\text{Bfl}} = 0^\circ$ in the limit of $\theta_{\text{scatt}} \ll 1/\Gamma_1$, where the particle momentum is stochastically deflected on arbitrarily small angular (and therefore temporal) scales. In such cases, particles diffuse in the region upstream of the shock only until their velocity’s angle to the shock normal exceeds around $1/\Gamma_1$, after which they are rapidly swept downstream of the shock. The lower kinematic energy gains in shock transits dominate higher shock-layer retention rates, and guarantee a steeper distribution under SAS conditions for $\Theta_{\text{Bfl}} = 0^\circ$ shocks; the monotonic steepening and loss of structure as θ_{scatt} declines is exhibited in [4] for ultra-relativistic shocks, and [19] for the mildly-relativistic domain.

Now the focus turns to the influence the effective frequency λ/r_g of scatterings, and the upstream field obliquity Θ_{Bfl} have on the accelerated population. Representative particle (electrons or ion) differential distributions dN/dp that result from the simulation of diffusive acceleration at mildly-relativistic shocks of speed $\beta_{1x} = 0.5$ are depicted in the *left panel* of Figure 2 (see [2, 4] for $\Gamma_1 \gg 1$ simulation results). Here, the subscript x denotes components along the shock normal. These distributions were generated for $\theta_{\text{scatt}} \lesssim 10^\circ$, i.e. in the SAS regime, for low magnetic fields corresponding to Alfvénic Mach numbers $M_A \gg 1$, and in the NIF frame. Results are displayed for two different upstream fluid frame field obliquities, namely $\Theta_{\text{Bfl}} = 48.2^\circ$ and $\Theta_{\text{Bfl}} = 59.1^\circ$, with corresponding de Hoffman-Teller (HT [21]) frame dimensionless speeds of $\beta_{\text{HT}} = \beta_{1x}/\cos \Theta_{\text{Bfl}} = 0.75$ and 0.975 , respectively. *Subluminal* shocks are those where the HT flow speed β_{HT} corresponds to a physical speed, less than unity, i.e. the upstream field obliquity satisfies $\cos \Theta_{\text{Bfl}} < \beta_{1x}$. When $\beta_{\text{HT}} > 1$, the de Hoffman-Teller frame does not exist, and the shock is said to be *superluminal*. See the right hand panel of Fig. 1 for the HT frame shock geometry. The distributions clearly exhibit an array of indices σ , including very flat power-laws, that are not monotonic functions of either the field obliquity Θ_{Bfl} nor the key diffusion parameter $\eta = \lambda/r_g$. These properties are illustrated in the *right panel* of Fig. 2, where it is also evident that the distributions are generally steeper in superluminal shocks [2] with $\lambda/r_g \gtrsim 10$. The left panel of Fig. 2 also emphasizes that the normalization of the power-laws relative to the low momentum thermal populations is a strongly-declining function of λ/r_g . This is a consequence of a more prolific convection of suprathermal particles downstream of the shock that suppresses diffusive injection from thermal energies into the acceleration process. Such losses are even more pronounced when $\lambda/r_g \geq 10^4$, to the point that acceleration is not statistically discernible for $\beta_{\text{HT}} > 0.98$ runs with 10^4 simulated particles. This feature is salient for the discussion on astrophysical sources below.

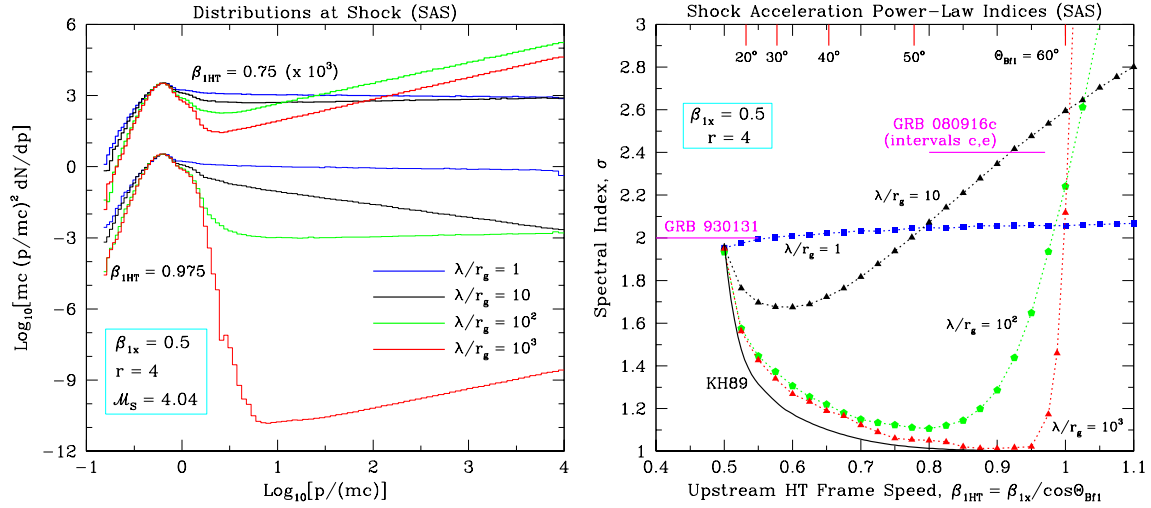


FIGURE 2. *Left panel:* Particle distribution functions dN/dp (scaled by p^2) from mildly-relativistic sub-luminal shocks ($\Gamma_{1x}\beta_{1x} = 0.577$, i.e. $\beta_{1x} = u_{1x}/c = 0.5$) of upstream-to-downstream velocity compression ratio $r = u_{1x}/u_{2x} \approx 4$. Simulation results are depicted for two de Hoffman-Teller frame upstream flow speeds $\beta_{\text{HT}} = \beta_{1x}/\cos\Theta_{\text{Bf1}}$. These are in distinct groups of four: $\beta_{\text{HT}} = 0.75$ (upstream magnetic field obliquity $\Theta_{\text{Bf1}} = 48.2^\circ$, multiplied by 10^3) for the upper four histograms, and $\beta_{\text{HT}} = 0.975$ (i.e., $\Theta_{\text{Bf1}} = 59.1^\circ$) for the lower four histograms. Scattering off hydromagnetic turbulence was modeled by randomly deflecting particle momenta by an angle within a cone, of half-angle θ_{scatt} , whose axis coincides with the particle momentum prior to scattering; four different ratios of the diffusive mean free path λ to the gyroradius r_g were adopted for each Θ_{Bf1} . All results were for small angle scattering (SAS), when $\theta_{\text{scatt}} \lesssim 1/\Gamma_1$ and the distributions become independent of the choice of θ_{scatt} .

Right panel: Power-law indices σ for simulation runs in the limit of small angle scattering (pitch angle diffusion), for mildly-relativistic shocks of upstream flow speed $\beta_{1x} \equiv u_{1x}/c = 0.5$, and an MHD velocity compression ratio $r = 4$. The indices are displayed as functions of the effective de Hoffman-Teller frame upstream flow speed $\beta_{\text{HT}} = \beta_{1x}/\cos\Theta_{\text{Bf1}}$, with select values of the fluid frame field obliquity Θ_{Bf1} marked at the top of the panel. The displayed simulation index results were obtained for different diffusive mean free paths λ parallel to the mean field direction, namely $\lambda/r_g = 1$ (squares), $\lambda/r_g = 10$ (triangles), $\lambda/r_g = 10^2$ (pentagons), and $\lambda/r_g = 10^3$ (triangles), as labelled. The lightweight curve at the bottom labelled KH89 defines the semi-analytic result from Kirk & Heavens' [7] solution to the diffusion-convection equation, corresponding to $\lambda/r_g \rightarrow \infty$. The short heavyweight lines labelled GRB 930131 (EGRET detection) and GRB 080916c (*Fermi* detection) indicate the approximate spectral index σ that is appropriate for these gamma-ray bursts, if a cooled synchrotron emission scenario is operable.

The existence of very flat distributions in the subluminal domain for very large λ/r_g is a remarkable feature of Figure 2. This phenomenon was identified by Kirk & Heavens [7] in their eigenfunction solution technique [6] for the diffusion-convection equation, which was restricted to subluminal, oblique shocks. Results for their $\beta_{1x} = 0.5$ analysis are presented as the solid curve labelled KH89 in the right panel of the Figure. Clearly, the Monte Carlo indices closely approach those of the semi-analytic method of [7] for $\lambda/r_g = 10^3$, an agreement that is improved slightly when λ/r_g is increased to 10^4 . Yet there are differences between the two approaches, and these yield the expected slight discrepancies in spectral index determination. The method of [7], being tantamount to a guiding center technique, employs conservation of the magnetic moment

$p^2(1 - \mu^2)/(2B)$ for particle-shock interactions when determining transmission and reflection probabilities of charges, naturally differing from gyro-orbit determinations of these probabilities. This nuance probably seeds the different values of σ derived in the two approaches, which, as expected, are small when shocks are effectively parallel, and highly oblique. More details of the comparison of these approaches are discussed in [16], which provides an extended exposition on the implementation of the Monte Carlo code, its validation and many of its key acceleration results. It can also be noted that comparing with the indices derived by [7] was the major motivation behind the artificial choice of the compression ratio $r = 4$, which is somewhat larger than the Rankine-Hugoniot MHD value for $\beta_{1x} = 0.5$, $M_s = 4.04$ conditions. Also, a low sonic Mach number M_s was chosen so as to maximize the efficiency of injection from thermal energies.

The Action of Shock Drift Acceleration

The origin of these flat indices is elucidated by the parameter survey here, and more specifically by the inclusion of cross field diffusion in the Monte Carlo simulations. Diffusive transport of particles perpendicular to the mean field was omitted in the analysis of [7], a restriction that is the primary reason for σ dropping below two. This is clearly evident from the right panel of Figure 2, which indicates that $\sigma \lesssim 1.5$ scenarios are realized only for $\lambda/r_g \gtrsim 10^2$, i.e. laminar fields and almost pure gyrotational motion. The primary origin of the acceleration is then connected to coherence in the shock layer. To provide further insight, individual particle trajectories were tracked in the Monte Carlo runs, and those exhibiting profound energy gains isolated. One such example is provided in Fig. 3, together with its corresponding momentum trace (right panel); the particles were injected with superthermal momenta $p = 5mc$ to circumvent any injection problems. Diffusion has minimal impact on the gyrotational motion in the left panel. The trajectories are 2D projections, and the pitch angle is evolving almost adiabatically in the particle-shock interaction to preserve gyrotational coherence. The momentum histories in the right hand panel more readily highlight the property that the acceleration is directly coupled to periods when the particle's gyration straddles the shock. Moreover, inertial motion in the y or $\mathbf{u} \times \mathbf{B}$ direction accompanies these epochs of energization. These two characteristics are the hallmarks of *shock drift acceleration* (SDA).

The acceleration of particles in the drift electric fields associated with oblique shock discontinuities has been extensively studied in non-relativistic contexts [22, 23, 24, 25, 26]. The origin of the effect is the net work done on a charge by the Lorentz force in a zone of non-uniform magnetic field. The principal equation governing this is

$$\mathbf{p} \cdot \frac{d\mathbf{p}}{dt} = q\mathbf{p} \cdot \left\{ \mathbf{E} + \frac{\mathbf{v}}{c} \times \mathbf{B} \right\} \equiv q\mathbf{p} \cdot \mathbf{E} \quad , \quad (1)$$

where \mathbf{E} is the $\mathbf{u} \times \mathbf{B}$ drift field that exists in any oblique shock rest frame other than the HT frame. In the uniform \mathbf{B} fields either upstream or downstream, the energy gains and losses acquired during a gyroperiod exactly cancel, so that no net work is done, $dW = 0$. In contrast, when a charge's gyromotion straddles the shock discontinuity, the sharp field gradient induces an asymmetry in the time spent by the charge either side of the shock,

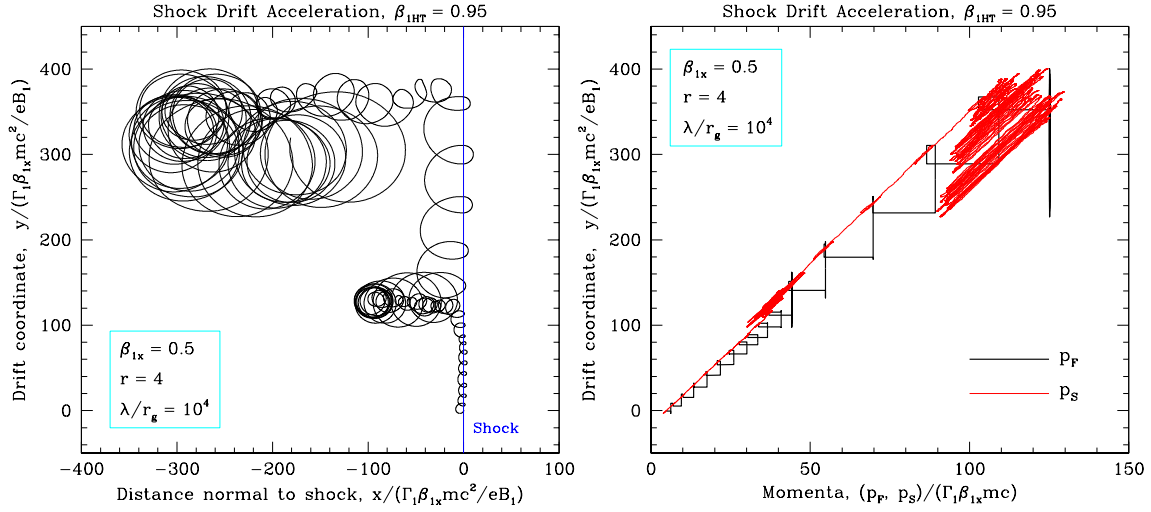


FIGURE 3. *Left panel:* A portion of a shock-layer trajectory for a selected particle accelerated from low to high energies, illustrating two key features of shock drift acceleration: coherent trapping in the shock, and occasional upstream excursions. The projection is onto the x - y plane, where the $\mathbf{u} \times \mathbf{B}$ drifts lie in the y -direction. The shock speeds are as in Fig. 2; the large value of $\lambda/r_g = 10^4$ is adopted to generate the requisite conditions for coherent interaction with the shock. In this projection, energy gains incurred while the particle’s gyrations straddle the shock only become obvious when its pitch angles are altered in upstream transits. Particles that undergo these trajectories are rare, but populate the power-law tail. *Right panel:* The coupling between the fluid frame (p_F) and NIF shock rest frame (p_S) momenta of the particle selected in the left panel, and the drift coordinate y . The shock frame momentum evinces oscillatory behavior during upstream excursions, and both p_F and p_S display the linear trend with drift y that is characteristic of shock drift acceleration. The fluid frame momentum exhibits a “rectangular hysteresis” while the particle gyrates in the shock layer.

so that energy gains and losses do not negate each other. The compressive nature of the field discontinuity biases the net work done to positive increments in shock encounters between upstream excursions, and it is simply shown [23, 25] that $dW = qE_y dy$, i.e. this energy gain scales linearly with displacement along the drift coordinate y . This is the punchline of the right panel of Fig. 3, where y effectively represents a time coordinate during shock drift episodes, with $dW/dt = qE_y/c$. It is also noteworthy that interspersed between these acceleration periods are upstream excursions where infrequent scattering slowly tries to isotropize the pitch angles, a feature clearly identified for the SDA phenomenon at non-relativistic shocks [26]. Particles that participate in the SDA initially have HT frame pitch angle cosines μ_{HT} considerably less than unity, so as to satisfy the reflection criterion: therefore they are rare in near-luminal shocks, for which the incident upstream angular distribution is highly-beamed around $\mu_{HT} \sim 1$. During upstream excursions that follow reflection, the particles tend to get swept back to the shock as soon as they are deflected and acquire momenta outside their Lorentz cone, i.e. before reaching isotropy in the upstream fluid frame. Therefore, in these $\lambda/r_g \gg 1$ cases, μ_{HT} continues to satisfy the reflection criterion during these brief upstream epochs. The repetition of SDA and upstream excursions, i.e. trapping in and near the shock, is therefore virtually guaranteed once the initial reflection is realized for a select particle.

This investigation provides an identification of the significance of shock drift acceleration in controlling σ for relativistic shocks. The reason it couples to unusually flat distributions ($\sigma < 1.5$) revolves around extremely efficient trapping in the shock layer, which permits repeated episodes of SDA in select particles with appropriately-tuned gyro-phases at the onset of shock-orbit interactions. The combination of the rapid energization rate, upstream hiatuses in SDA, and a slow leakage rate downstream leads naturally [27] to an approximate $dN/dp \propto p^{-1}$ distribution. But only when $\lambda/r_g \gtrsim 10^3$. The introduction of turbulence easily disrupts the coherence and precipitates efficient convection downstream [27], quenching the effectiveness of SDA. The result then is a dominance of shock drift acceleration contributions by first order Fermi (turbulent) ones when $\lambda/r_g \lesssim 30$. More importantly, when $\lambda/r_g \gtrsim 10$, an inexorable sweeping of charges downstream in superluminal shocks overpowers both acceleration contributions and steepens the spectrum dramatically, as is evident in the right panel of Fig. 2.

ASTROPHYSICAL SOURCE CONTEXT

The shock acceleration theory results presented in the previous Section can now be interpreted in the light of observations of astrophysical sources. The first class of germane sources consists of gamma-ray bursts (GRBs), whose prompt emission is generally observed in the 10 keV - 10 GeV range, with a characteristic spectral break around 200 keV to 1 MeV. Above this break, the spectrum is generally (but not always) an extended power-law $dn_\gamma/d\varepsilon_\gamma \propto \varepsilon_\gamma^{-\alpha_h}$. The focus here is on the relationship between the high energy spectral index α_h and the underlying particle acceleration conditions. This forges a direct connection to data from CGRO's EGRET telescope, and now to the growing database of *Fermi* LAT burst detections. The EGRET α_h index distribution [28] is constituted by a handful of sources with indices scattered in the range $2 \lesssim \alpha_h \lesssim 3.7$, with brighter bursts' indices concentrated in the range $\alpha_h \lesssim 2.8$, as tabulated in [29]. The recent *Fermi* detection [30] of GRB 080916c in both the GBM and LAT instruments offered an index of $\alpha_h \sim 2.2$ at energies above ~ 2 MeV in its most luminous epoch, and a steeper spectrum ($\alpha_h \gtrsim 2.5$) at other times. It is then evident that observationally, shock acceleration models must accommodate a radiation spectral index in the range $2 \lesssim \alpha_h \lesssim 4$ in order to be viable. Moreover, they must reasonably account for the spectral variability identified in GRB 080916c, i.e. fluctuating α_h values in a given source.

If one presumes that these photon spectra result from synchrotron emission that rapidly cools the radiating electrons, a popular paradigm [31, 32, 33] for the production of the prompt emission, then $\alpha_h = (\sigma + 2)/2$ for electron acceleration populations $dN/dp \propto p^{-\sigma}$. The σ corresponding to the values of $\alpha_h = 2.0$ for the flat-spectrum EGRET burst GRB 930131 and $\alpha_h = 2.2$ for GRB 080916c for time intervals (c,e) [30] are marked on the right panel of Fig. 2. It then becomes clear that the emission in GRB 930131 is consistent with acceleration at subluminal shocks and relatively near the Bohm diffusion limit. In contrast, the slightly steeper GRB 080916c spectrum is better explained by mildly superluminal shocks in the 60° - 70° obliquity range, but only if the scattering is strong, i.e. $\lambda/r_g \lesssim 3 - 10$. If, instead, synchrotron cooling is inefficient, the photon differential spectral index given by $\alpha_h = (\sigma + 1)/2$. Then the injected distribution must have an index σ higher by unity than that for cooling models,

in order to match the burst observations. This is a profound difference in that it moves the viable shock parameter space into the superluminal range, i.e. at higher field obliquities, and Bohm-limited diffusion is observationally excluded. No bursts have so far evinced extended power-law spectra flatter than $\alpha_h \approx 1.95$, absolving the need for acceleration in shocks with extremely low turbulence, i.e. $\lambda/r_g \gtrsim 10^2$ regimes. This is fortunate, since, from the left panel of Fig. 2, such shocks are inherently inefficient accelerators. Moreover, the generation of field turbulence is a natural part of dissipation in shocks, so that almost laminar fields are not expected, nor observed in *in situ* magnetometer measurements at heliospheric shocks (e.g. [34, 35] and references therein).

The second relevant astrophysical context concerns blazars, the subset of active galactic nuclei possessing relativistic jets of material emanating from the supermassive black holes at their centers; these jets are oriented virtually towards the observer. These have been the preserve of gamma-ray experiments ever since their discovery by EGRET [36], and subsequent observation by ground-based Cherenkov telescopes at TeV energies [37]. The TeV-band signals typically exhibit steep photon spectra (e.g. Mkn 421: [38, 39]) that include the absorption due to pair producing interactions $\gamma\gamma \rightarrow e^+e^-$ with infra-red and optical light generated by the intergalactic medium along the line of sight to the observer. The correction for this attenuation (so called *de-absorption*), leads to the inference of extremely flat particle distributions in energetic gamma-ray blazars (see for example [4]), with indices as low as $\sigma \sim 1.0 - 1.5$ in high redshift sources. To accommodate these observational constraints would require subluminal shocks with very modest or low turbulence levels. Yet, such inferences are based upon measurements in a limited waveband subject to profound absorption. More improved diagnostics are now enabled by *Fermi* LAT detections of blazars, which extend the observational window over a much larger energy range, nominally from 100 MeV to over 1 TeV, and most crucially, below the attenuation window. Accordingly, *Fermi* observations can more directly probe the underlying radiating particle population. A prime example of this is the multi-wavelength campaign on the PKS 2155-304 blazar [40] in a non-flare state, whose combined *Fermi*-*HESS* spectrum from 300 MeV to 3 TeV indicates an unattenuated photon spectral index of $\alpha_h \sim 1.6$, steepening to $\alpha_h \sim 2.0$ above 1 GeV. For a standard inverse Compton scattering interpretation with insignificant radiational cooling, this translates to an electron power-law index in the range $\sigma \sim 2.2 \rightarrow 3.0$, so that acceleration at mildly superluminal oblique shocks should provide the best description.

CONCLUSIONS

This paper has investigated some of the key characteristics of particle acceleration at relativistic shocks, including the identification of the role of shock drift acceleration in generating flat distributions in mildly-relativistic, subluminal shocks. It has also explored the connection between the acceleration process and high energy emission in two classes of astrophysical sources, namely gamma-ray bursts and jets in blazars. The simulation results presented clearly highlight the non-universality of the index of energetic, non-thermal electrons and ions, spawned by the variety of shock obliquities and the character of hydromagnetic turbulence in their environs. This non-universality poses no problem for modeling GRB or blazar high-energy power-law indices, though obser-

vations generally constrain the parameter space to subluminal or highly-turbulent and modestly superluminal shocks not far from the Bohm diffusion limit. Diffusive acceleration at ultra-relativistic shocks requires $\delta B/B \sim 1$ in order to generate sufficiently low σ to mesh with observed source photon spectra. It is unclear whether conditions in bursts and blazars can support such levels of turbulence at shocks embedded in their relativistic outflows, though it should be noted that large field fluctuations naturally emerge in PIC simulations of Weibel instability-driven relativistic shocks. It is anticipated that the rich prospects for *Fermi* gamma-ray observations of blazars and GRBs in the next few years will enhance our understanding of particle acceleration in their environs.

REFERENCES

1. Ellison, D. C., Jones, F. C. & Reynolds, S. P. 1990, *ApJ*, 360, 702.
2. Ellison, D. C. & Double, G. P. 2004, *Astroparticle Phys.*, 22, 323.
3. Niemiec, J., & Ostrowski, M. 2004, *ApJ*, 610, 851.
4. Stecker, F. W., Baring, M. G. & Summerlin, E. J. 2007, *ApJ*, 667, L29.
5. Baring, M. G. 2004, *Nucl. Phys. B*, 136C, 198.
6. Kirk, J. G. & Schneider, P. 1987, *ApJ*, 315, 425.
7. Kirk, J. G. & Heavens, A. F. 1989, *M.N.R.A.S.*, 239, 995.
8. Kirk, J. G., Guthmann, A. W., Gallant, Y. A., Achterberg, A. 2000, *ApJ*, 542, 235.
9. Hoshino, M., Arons, J., Gallant, Y. A. & Langdon, A. B. 1992 *ApJ*, 390, 454.
10. Nishikawa, K.-I., et al. 2005, *ApJ*, 622, 927.
11. Medvedev, M. V., et al. 2005, *ApJ*, 618, L75.
12. Spitkovsky, A. 2008, *ApJ*, 682, L5.
13. Jones, F. C. & Ellison, D. C. 1991, *Space Sci. Rev.* 58, 259.
14. Summerlin, E. J. & Baring, M. G. 2006, *Adv. Space Res.*, 38(7), 1281.
15. Ellison, D. C., Baring, M. G. & Jones, F. C. 1995, *ApJ* 453, 873.
16. Summerlin, E. J. & Baring, M. G. 2009, *ApJ*, in preparation.
17. Forman, M. A., Jokipii, J. R. & Owens, A. J. 1974, *ApJ* 192, 535.
18. Baring, M. G. 1999, in *Proc. of the 26th ICRC, Vol. IV*, p. 5, [[astro-ph/9910128](#)].
19. Baring, M. G. 2009, in *Proc. 6th Huntsville GRB Symposium*, eds. C. A. Meegan, et al., N. Gehrels, & C. Kouveliotou (AIP Conf. Proc. 1133, New York) p. 294
20. Bednarz, J. & Ostrowski, M. 1998, *Phys. Rev. Lett.*, 80, 3911.
21. de Hoffman, F. & Teller, E. 1950, *Phys. Rev. D*, 80, 692.
22. Sarris, E. T., & Van Allen, J. A. 1974, *J. Geophys. Res.*, 79, 4,157.
23. Jokipii, J. R. 1982, *ApJ*, 255, 716.
24. Pesses, M. E., Decker, R. B. & Armstrong, T. P. 1982, *Space Sci. Rev.* 32, 185.
25. Webb, G. M., Axford, W. I. & Terasawa, T. 1983, *ApJ*, 270, 537.
26. Decker, R. B. & Vlahos, L. 1986, *ApJ*, 306, 710.
27. Baring, M. G. & Summerlin, E. J. 2009, *Adv. Space Res.*, in preparation.
28. Dingus, B. L. 1995, *Astr. Space Sci.*, 231, 187.
29. Baring, M. G. & 2006, *ApJ*, 650, 1004.
30. Abdo, A. A., et al. (the *Fermi* Collaboration) 2009, *Science*, 323, 1688.
31. Rees, M. J. & Mészáros, P. 1992, *M.N.R.A.S.*, 258, 41P.
32. Piran, T. 1999, *Phys. Rep.*, 314, 575.
33. Mészáros, P. 2002, *Ann. Rev. Astron. Astr.*, 40, 137.
34. Balogh, A., et al. 1995, *Space Sci. Rev.* 72, 171.
35. Baring, M. G., Ogilvie, K. W., Ellison, D., & Forsyth, R. 1997, *ApJ*, 476, 889.
36. Hartman, R. C., Bertsch, D. L., Fichtel, C. L., et al. 1992, *ApJ*, 385, L1.
37. Punch, M., Akerlof, C. W., Cawley, M. F., et al. 1992, *Nature*, 358, 477.
38. Krennrich, F., Bond, I. H., Bradbury, S. M., et al. 2002, *ApJ*, 575, L9.
39. Aharonian, F., Akhperjanian, A. G., Beilicke, M., et al. 2003, *Astron. Astrophys.*, 410, 813.
40. Aharonian, F., Akhperjanian, A. G., Anton, G., et al. 2009, *ApJ*, 696, L150.